Melt Pond Fraction Derived From Sentinel-2 Data: Along the MOSAiC Drift and Arctic-wide

Hannah Niehaus[1], Gunnar Spreen[1], Gerit Birnbaum[2], Larysa Istomina[2], Evelyn Jäkel[3], Felix Linhardt[4], Niklas Neckel[2], Niels Fuchs[5], Marcel Nicolaus[2], Tim Sperzel[3], Ran Tao[2], Melinda Webster[6], Nicholas Wright[7]

[1]Institute of Environmental Physics, University of Bremen, Bremen, Germany
[2]Helmholtz-Zentrum für Polar- und Meeresforschung, Alfred-Wegener-Institut Bremerhaven, Germany
[3]Faculty of Physics and Earth Science, Leipzig University, Leipzig, Germany
[4]Institut für Geographie, Christian-Albrechts-Universität zu Kiel, Kiel, Germany
[5]Institute of Oceanography, University of Hamburg, Hamburg, Germany
[6]Geophysical Institute, University of Alaska Fairbanks, Fairbanks, Alaska, USA
[7]Thayer School of Engineering, Dartmouth College, Hanover, NH, USA

Key Points:

- Algorithm to extract melt pond and open water areas from Sentinel-2 imagery with minimum accuracy of 6 %
- Exceptional early melt pond formation on MOSAiC Central Observatory, summer 2020, compared to broader vicinity
- We demonstrate high spatial and temporal variability of melt pond fraction on local and regional scales

Plain Language Summary

In the Arctic summer, puddles of surfaces melt water, called melt ponds, form on the sea ice. These melt ponds reduce the ability of the surface to reflect the sunlight. Instead, they absorb more solar energy and pave the way into the ocean beneath where the energy is also absorbed. Thus, it is important to know where these melt ponds develop and what fraction of the surface they cover. To investigate this, we present a classification algorithm that is used to extract the areal fraction of melt ponds from satellite measurements. The special focus of this study is the MOSAiC campaign in summer 2020, where the research vessel Polarstern drifted with one ice floe for one year. We can see a separation of this floe into two parts. One of them shows melt pond formation much earlier than the other. This is because of different ice age and surface properties. Additionally, we use the classification algorithm to analyze the differences of melt pond fraction between different dates and regions in the Arctic.

Corresponding author: Hannah Niehaus, `niehaus@uni-bremen.de`

Abstract

Melt ponds forming on Arctic sea ice in summer significantly reduce the surface albedo and impact the heat and mass balance of the sea ice. Their seasonal development features fast and local changes in fractions of surface types, demonstrating the necessity of improving melt pond fraction (MPF) products. We present a renewed method to extract MPF from Sentinel-2 satellite imagery, which is evaluated by MPF products from higher resolution satellite and helicopter-borne imagery. The analysis of melt pond evolution during the MOSAiC campaign in summer 2020, shows a split of the Central Observatory (CO) into a level ice and a highly deformed part, the latter of which exhibits exceptional early melt pond formation compared to the vicinity. Average CO MPFs amount to 17 % before and 23 % after the major drainage. Arctic-wide analysis of MPF for years 2017-2021 shows a consistent seasonal cycle in all regions and years.

1 Introduction

During the Arctic summer, melting of snow and sea ice forms pools of melt water on top of the sea ice (Untersteiner, 1961). The areal fraction covered by these melt ponds exhibits high temporal and spatial variability (D. Perovich et al., 2002; Polashenski et al., 2012). Peak melt pond fractions (MPFs) of 60 to 80 % (Maykut et al., 1992; Eicken et al., 2004) depending on ice type, topography, and location (Polashenski et al., 2012) have been observed. Typical values of MPFs in summer in the central Arctic range from 15 to 40 % (Rösel & Kaleschke, 2011; Istomina et al., 2015b). Melt ponds on sea ice significantly reduce its broadband and spectral albedo (Malinka et al., 2018; Pohl et al., 2020; Light et al., 2022) affecting the heat and mass balance due to an increase of solar absorption within and an enhancement of transmission through the ice into the Arctic ocean (Light et al., 2008; Nicolaus et al., 2012). However, global climate models still lack a decent representation of melt ponds (Hunke et al., 2013; Flocco et al., 2010; Dorn et al., 2018). This is caused by the complexity and variability of melt pond formation and evolution and its mismatch compared to observational scales.

There are numerous efforts to enhance the understanding of melt pond physics based on in-situ (Eicken et al., 2002; Light et al., 2008; Nicolaus et al., 2012), air-borne (D. Perovich et al., 2002; Miao et al., 2015; Buckley et al., 2020), and high resolution ($\mathcal{O}$(m)) satellite measurements (Markus et al., 2002; Rösel & Kaleschke, 2011; Istomina et al., 2015b; Li et al., 2020; Wang et al., 2020). Due to the limited availability of observational data, the available studies focus on case studies and are often used for validation purposes of medium and low resolution satellite observations, which cover larger areas and longer time periods (Rösel et al., 2012; Zege et al., 2015; Lee et al., 2020; Wright & Polashenski, 2020; Peng et al., 2022).

Wang et al. (2020) have developed an algorithm to extract MPF from small subsets of optical satellite measurements from the Copernicus Sentinel-2 mission. We have generalized this algorithm, which enables the application to extended regions and a larger sample of datasets. Using the generalized approach, we (1) analyz the MPF along the track of the Multidisciplinary drifting Observatory for the Study of Arctic Climate (MOSAiC) from June 14 (Figure S4) to July 27 2020, (2) enlarged the available datasets of MPF in the Arctic for, e.g. validation purposes of lower resolution MPF products or evaluation of models, and (3) studied the local and temporal variability of MPF in the Arctic.

2 Study Sites and Datasets

2.1 Study Sites

In 2019-2020, the year-long Arctic research expedition MOSAiC of the research vessel *Polarstern* measured and analyzed sea ice, atmospheric, ocean, bio-geochemical, and ecological processes throughout a full seasonal cycle (Nicolaus et al., 2022; Shupe et al., 2022; Rabe et al., 2022). Comprehensive observational data of the snow and ice conditions were collected at the MOSAiC Central Observatory (CO) (Krumpen et al., 2021; Nicolaus et al., 2022) in winter and spring 2019-2020. Thus, an analysis of MPF evolution in the subsequent summer period is of special interest (Thielke et al., 2022). Webster et al. (2022) present a detailed analysis of melt pond evolution on the MOSAiC CO primarily based on in-situ transect measurements. Krumpen et al. (2021) show first insights into optical satellite imagery of the CO. We expand on these investigations by analysing the full available Sentinel-2 dataset covering the drifting position of the MOSAiC CO, from June to July 2020. For the investigation of the classification algorithm performance and the presentation of pan-Arctic MPF variability, satellite measurements of other locations are included into our analysis for 2017 to 2021.

2.2 Sentinel-2 Satellite Imagery

We use Top-of-Atmosphere (TOA) reflectances supplied by the Sentinel-2A and 2B satellites operated by the European Space Agency (`https://scihub.copernicus.eu/dhus/`). The satellites provide coverage of latitudes up to 82.8 ° with a swath of 290 km and revisit time of five days. However, the availability of suitable scenes is compromised by prevalent cloud contamination typical for the Arctic summer. Both, the latitude limit and clouds, strongly restrict the number of available Sentinel2 scenes during MOSAiC. The MultiSpectral Instrument (MSI) measures TOA radiances in 13 spectral bands in the optical and near infrared (NIR) range (440-2200 nm) with a spatial resolution of 10 m to 60 m. These are post-processed to Level-1C (L1C) TOA reflectances, which are provided in orthorectified quality with correction for the disparity of the incoming solar radiation defined by the solar zenith angle and a distinctive cloud mask.

For this study, only Sentinel-2 scenes with internal cloud percentage of less than 1 % are taken into account. In additions, scenes with potential thin cirrus clouds or dust are discarded manually. Furthermore, a combination of bands 8 and 11 (842 nm and 1610 nm) is used to check for cloud contamination following criteria described by Istomina et al. (2010). As a result, the initially selected 43 scenes are reduced to 31.In two cases (July 7 and July 27) a manual correction is applied to account for a constant offset due to homogeneous contamination. The pool of suitable Sentinel-2 imagery is split up into one part (10 scenes) used for the development of the classification algorithm, and another (21 scenes) applied for unbiased testing. An overview of all scenes used, their acquisition times, locations and purposes can be found in Table S5.

2.3 OSSP Melt Pond Product from SkySat Satellite Imagery

One product used for the classification algorithm evaluation is based on high resolution (0.5 m) satellite imagery obtained by the Planet SkySat (courtesy of Planet Labs, Inc.) satellite platform. The SkySat mission comprises 21 satellites circling in a non-sun-synchronous orbit at an altitude of 450 km to achieve a spatial resolution of 0.5 m of the orthorectified product, which has a minimum swath width of 5.5 km. The data contain measurements of the reflected radiance in four spectral bands. These cover the wavelengths required for RGB imagery and the NIR. Based on the Open Source sea ice Processing (OSSP) algorithm (Wright & Polashenski, 2019), Wright et al. (2021) provide a classification of this data into four surface type classes: (1) open water, (2) melt ponds and submerged ice, (3) thin ice and (4) thick ice. For the comparison with the Sentinel-2 data, classes (3) and (4) are combined to one sea ice class, (2) corresponds to the melt pond class. Hereinafter, the MPF derived from the SkySat imagery by the use of the OSSP algorithm is referred to as *SkySat* MPF.

2.4 Airborne Imagery based Melt Pond Product

The helicopter-borne sea ice surveys conducted during the summer of the MOSAiC campaign provide high resolution RGB imagery acquired with a Canon EOS 1D Mark III camera with wide-angle lense. This imagery is stitched and provided as orthomosaics with a resolution of 0.5 m (Neckel et al., 2022). The main classes deduced from the RGB imagery are (1) open water, (2) melt ponds, (3) submerged ice and (4) snow and ice. For our purpose classes (2) and (3) are summarized as "melt pond" class for the comparison with the products derived from SkySat and Sentinel-2 satellite imagery and class (4) corresponds to the "ice class". Hereinafter, the MPF derived from the classification of the helicopter-borne imagery is referred to as *Helicopter* MPF. The estimated error of the "Helicopter" MPF is 2 %. Further information about the processing is given in supplementary Text S1.

3 Methodology

3.1 Classification of Sentinel-2 Imagery

Melt pond sizes on sea ice range from cm^2 to km^2 (D. Perovich et al., 2002) with a majority at widths and lengths that are smaller or in the range of the Sentinel-2 footprint of 10 m x 10 m pixel size. For this reason, a binary classification is not sufficient and a spectral unmixing approach is necessary to estimate the MPF. In this paper, MPFs are computed as the pond area divided by the ice (ponded plus not ponded) area.

The *LinearPolar* Algorithm by Wang et al. (2020) was developed for small subsets (less than 2 km edge length) of Sentinel-2 scenes to extract MPF from the optical imagery. We adopt the fundamental approach and introduce changes to make the algorithm applicable to larger subsets (larger than 50 km length) and a wider variability of scenes.

The algorithm is based on the bands 2 (*B2*) and 8 (*B8*) of the Sentinel-2 instrument with central wavelengths of 490 nm and 842 nm, respectively. This is because of the significant difference between the spectral behavior of ice, melt pond and open water surfaces at these wavelengths (Rösel et al., 2012; Wang et al., 2020). Whereas dry ice shows little changes in albedo for smaller wavelengths of the visible range (*B2*) and only a slight decrease towards the NIR (*B8*), melt ponds feature a strong drop in albedo towards larger wavelengths (Istomina et al., 2015a; Malinka et al., 2018). The liquid water content of the surface layer affects this albedo drop and thus leads to a substantial variability in the albedo of ice surfaces with different melt progress (Grenfell & Maykut, 1977; D. K. Perovich et al., 1996; Malinka et al., 2016). Open water shows almost no changes within the visible and near-infrared range with a constant low albedo of below 0.1 (Pohl et al., 2020). Based on these differences, the scatterplot in Figure 1 (a) displays three major modes. The most concise one is the open water mode with low values for both, *B2* and the difference between bands 2 and 8 (*B2-B8*), due to its constant spectral behavior. The largest mode presents all types of ice surfaces featuring a large variability due to the differences in liquid water content. However, there is a straight line defining an upper limit. Along this line the brightest pixels of pure, dry ice are located. The third mode exhibits another edge where the pixels with 100 % of ponds are aligned. Based on those modes two lines, named *ice axis* and *pond axis*, are defined serving as principal components for a polar coordinate transformation. Fixed axes are used for the whole dataset to ascertain a robust classification independent of the image details and subset size. The choice of the axes is conducted on the basis of a set of scenes, which comprise a variety of melt stages and feature different compositions of the surface constituents: ice, melt ponds and open water. The Sentinel-2 scenes used for defining the axes, and thus form the training dataset of the classification algorithm, are marked with a *D* in the *purpose* column in Table S5.

Subsequently, the two-dimensional Cartesian scatterplot is transformed into polar coordinates following the formulas specified by Wang et al. (2020). This leads to a parallelization of the two axes, as visualized in Figure 1 (b). θ is associated with the MPF of each pixel assuming a linear transition between the 100 % axes for ponds and ice. r relates to the different spectral behavior of darker and brighter ice surfaces or pond types. Thus, the distinct mode of dark, open water can be clearly identified at low values of r and a cutoff value for open water areas, marked by the vertical grey line, is defined. All pixels with values r smaller than the water cutoff value are set to zero MPF and are excluded from the assignment of MPF linearly depending on the value of θ. This yields an estimate of the open water area. The choice of the open water cutoff value can be clearly identified for every single scene. However, it can vary between scenes depending on the existence of open water and the dominant ice types. Therefore, a default value for the open water cutoff line after the polar coordinate transformation of $r = 0.35$ is set. The suitability of this threshold is checked for each sample individually. An adjustment in the range of 0.30 to 0.38 is made if there is a significant amount of pixels with $\theta >$ *pond axis* but $r <$ *water cutoff* that can not be assigned to open water areas. Hereinafter, the MPF derived from the Sentinel-2 imagery using the algorithm described here is referred to as "Sentinel-2" MPF.

3.2 Validation with High Resolution Imagery

The Sentinel-2 MPF is compared with MPFs derived from helicopter-borne and higher resolution SkySat satellite imagery, which both have a resolution of 0.5 m but are scaled down to the resolution of 10 m of Sentinel-2. For the collocation of the different datasets, the ice drift within the time offset between the acquisition times is approximated using the GNSS position of *Polarstern*. However, especially the shape of open water areas can change considerably even in short time periods. The position of the research vessel is then used as reference point to define the areas to be compared. Figure 1 displays the Sentinel-2 melt pond classification results in comparison with the MPF products from SkySat and airborne imagery for two dates, before and after the majority of melt ponds drained (Webster et al., 2022). In Figure S3, the comparison for July 7, where melting has progressed, is presented. The results shown in Figure 1 (c)-(f) combine June 30 (Sentinel-2 and Helicopter) and July 1 (SkySat). Sentinel-2 imagery is available for both days showing little changes. Thus the combination of these days for a pre-drainage comparison of melt pond classification results is feasible. The post-drainage MPFs all stem from the same day, July 22.

In both cases the dominant sea ice and pond features are clearly visible in all products and agree well with regard to the MPFs. It is evident that the higher resolution products resolve more small pond features even with the downsampled resolution shown here. This is the reason the histogram of Sentinel-2 MPF is showing a significantly higher peak at minimum MPF values before the drainage (Figure 1 (f)). After the drainage the probability for pixels with minimum MPF

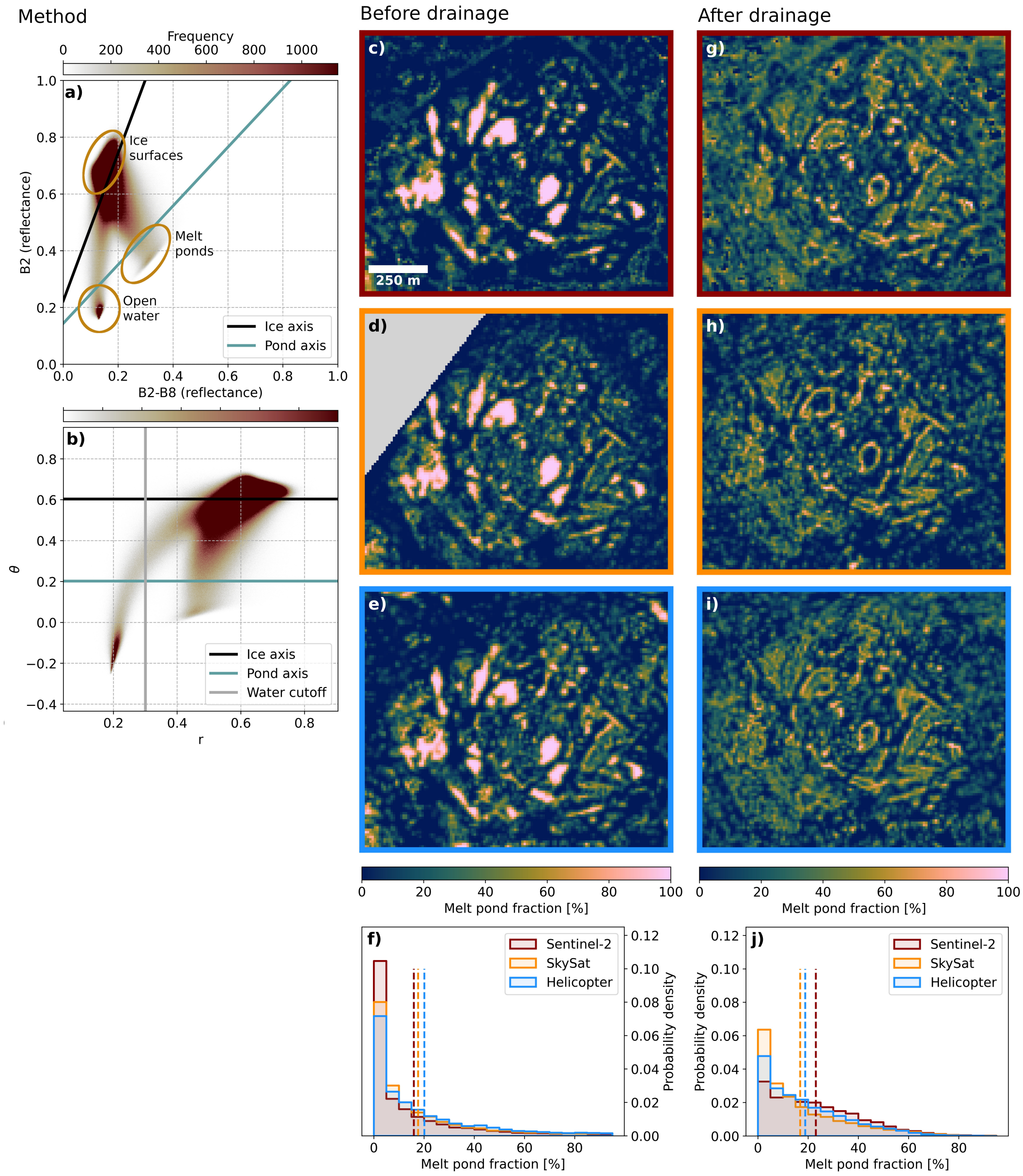

Figure 1. Left: Two-dimensional density plots of Sentinel-2 reflectances of (a) band 2 (*B2*) and the difference between bands 2 and 8 (*B2-B8*) and (b) the transformed coordinates r and θ. The color scale indicates the frequency of the appearance of value pairs. The ice and pond axes are marked in black and red, respectively, and the threshold for the open water cutoff is denoted by the grey vertical line in (b). This example shows the results for scene T31XEL on June 30, 2022. Middle and right: MPF maps derived from Sentinel-2 ((c) and (g)), SkySat ((d) and (h)) and Helicopter obsercations ((e) and (i)) and histograms of the MPF distributions ((f) and (j)). Panels (c)-(f) show measurements from June 30 (Sentinel-2 and Helicopter) and July 1 (SkySat), before the drainage of the ponds started. Panels (g)-(j) show measurements from July 22, after the major drainage period. The colored frames of the maps indicate the different datasets according to the colors in the histograms. The scalebar in panel (c) is valid for all maps.

values in the Sentinel-2 product is much lower than for the other products (Figure 1 (j)). Due to the overall shift of surface conditions from ice partly covered with distinct ponds to a water saturated surface with smaller dry ice areas, this is attributed to the resolution difference as well. With ponds draining, the surface conditions become more complex featuring small-scale alternation of wet ice, surface scattering layer (SSL), ponds and subnivean ponds (SSL with melt water visible below)(Webster et al., 2022; Smith et al., 2022) causing higher uncertainties. However, the agreement both visually as well as by statistics shown in the histograms is excellent with differences in mean smaller than 7 %. We conclude that implementing the above described classification algorithm to Sentinel-2 reflectance measurements is reasonable with an uncertainty increasing with time due to advancing small-scale features raised by pond drainage. The uncertainty of the product in general is estimated to be below 6 %, with smaller values, below 4 %, before melt ponds start draining.

4 Results and Discussion

4.1 Case Study - Melt Pond Fraction along MOSAiC Drift Track

Figure 2 (a) shows true color composites and their classification of all the Sentinel-2 observations with little or no cloud contamination along the MOSAiC drift track in summer 2020. The MPF maps are presented for the small segment of the MOSAiC CO (1.2 km x 1.4 km) and for an extended area of 3 km x 3.5 km centering the floe. On July 1 the extent of the cloud-free scene is limited. In Figure S4 four more dates with observations that are disturbed by clouds and thus not useful for quantitative analysis are displayed for the visual impression of MPF evolution.

At the time (June 21) of the first observation shown in 2 (a) the MOSAiC CO features already large, distinct melt ponds of different colors whereas the neighboring ice floes scarcely exhibit melt ponds. Unfortunately, earlier observations from Sentinel-2 are not available as the MOSAiC site was at latitudes higher than the limitations of the satellite mission. Webster et al. (2022) date the melt onset on the CO to May 25 accompanied by rainfall, followed by a period of freezing and fresh snowfall. However, this event pre-conditioned the surface for later pond formation, visible in the observations on June 18 (Figure S4), 21 and 22. In the first two columns in Figure 2 the true color composite and MPF maps for the latter two dates are presented. The mean values of MPF on the MOSAiC CO amount to 8 % and 9 % and in the vicinity to 2 % and 2 % for June 21 and 22, respectively. The vicinity is herein defined as the area shown in the bottom row excluding the CO floe area shown in the middle row. The difference between the melt pond development stages of the MOSAiC and neighboring floes is even more distinct in the inspection of the statistical distribution of MPF values, presented in Figure 2 (b). Both areas cover the full range of MPFs, however, with a strong emphasis on low MPF values and the distribution for the vicinity is much more narrow at low values. Interestingly, the MOSAiC CO is divided into two regions: one is featuring large melt ponds, the other is almost pond-free similar to the neighboring floes. This can be attributed to the ice thickness and surface conditions. It has been reported that the MOSAiC CO was characterized by strong deformations and high surface roughness in parts of the CO (Krumpen et al., 2021; Thielke et al., 2022; Nicolaus et al., 2022). This favors the early formation of melt ponds by accumulating melt water in the depressions (Webster et al., 2015). Thus, a division of the CO into two parts with highly deformed ice and more melt ponds, and more level-ice with less melt ponds in the early melting stage, as observed here, is reasonable.

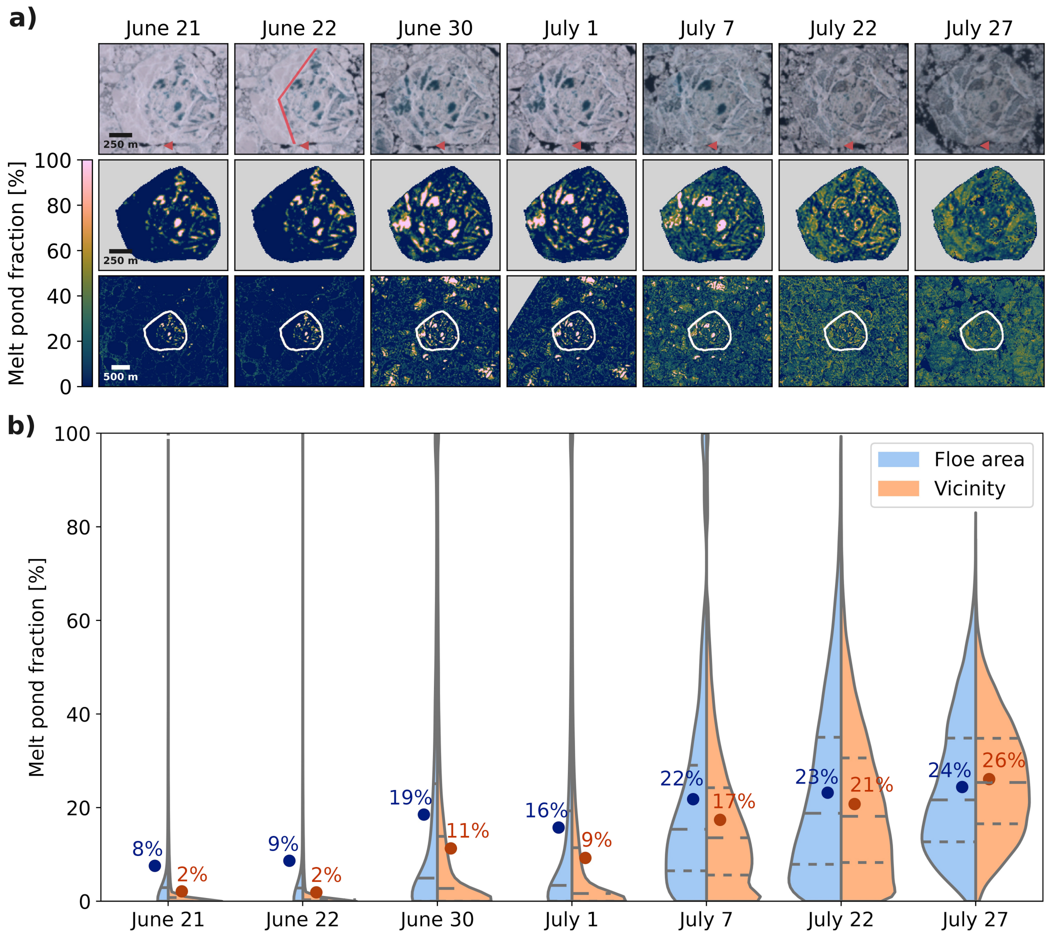

Figure 2. Melt pond fraction (MPF) evolution along the MOSAiC drift track. (a) Upper row: Sentinel-2 true color composites of the MOSAiC CO area defined relatively to Polarstern position marked by the red triangles. The red line on June 22 mark the observed split of the CO Middle row: MPF classification results in % for the CO. Bottom row: MPF maps of vicinity around the Polarstern vessel displayed in the same colorscale as above, the indicated CO area is excluded from the comparison. (b) Probability density functions of the MPF distribution for the floe area (blue) and vicinity (orange). The circles mark the mean MPFs for the two areas, with the values given aside. The dashed lines mark the medians and upper and lower quantiles.

About one week later, on June 30 and July 1, melt ponds have extended, the more leveled region of the MOSAiC CO is heavily ponded now and also the neighboring floes exhibit stronger pond formation. The overall appearance of the surface in the top row of Figure 2 (a) is less brightly, which may be attributed to the completed melt of snow by June 25 (Lei et al., 2022) and thus increased humidity of the surface. The distribution of MPF is broadend and for both areas, thinning above fraction values of 40 %. However, there is a slight increasing again at maximum values. The mean values on the MOSAiC CO amount to 19 % and 16 % and on the neighboring floes to 11 % and 9 % for June 30 and July 1, respectively. These differences between the two days and regions are below the estimated uncertainty of the product. However, the classification is self-contained. Thus, relative changes in between days may be detected even below the algorithm uncertainty.

July 7 is the last observation where large, distinct melt ponds are visible. However, ponds close to the floe edge already have drained. They become connected to the ocean by lateral channels, which enable the outflow of water while the more centered and isolated ponds remain intact (Polashenski et al., 2012; Webster et al., 2022). By July 18 (Figure S4) and latest July 22 all large melt ponds have drained and split into multiple smaller ponds due to the development of vertical drainage channels (Flocco et al., 2010; D. Perovich et al., 2021). Most of them can not be separated anymore at the resolution of 10 m, which darkens the overall appearance of the ice resulting in a broad MPF distribution during this later melt stage. Webster et al. (2022) report the major drainage period between July 10 and 12, which would cause a MPF reduction. On the other hand Lei et al. (2022) report an increase of surface equivalent ice/snow melt between July 10 and 20 of +0.14 m. This is in agreement with the observation of exceptional warm and moist conditions in summer 2020 (Rinke et al., 2021). Thus, meltwater outflow and formation are strongly counteracting, the latter of which prevails leading to a slight increase of the mean MPF in the period from July 7 to 27. However, the distribution of MPF values is changing significantly. Fully pond covered pixels diminish as well as those pixels with no ponds at all. The ice gets water saturated leading to an overall darkening of the surface (Eicken et al., 2002; Webster et al., 2015).

4.2 Spatial and Temporal Melt Pond Fraction Variability

With our classification method the spatial variability of MPF can also be analyzed on a larger scale. Figure 3 presents the mean MPF values of a set of 30 Sentinel-2 observations at different times and locations in the Arctic. An overall start of pond formation in the second half of June or early in July is visible with considerably increasing MPFs in the first week of July in all three regions: Canadian Arctic, Fram Strait, and Siberian Arctic. The distribution peaks around July 8 and decreases quickly first and more slowly towards late summer. However, this views all years and locations together featuring a large variability in meteorological conditions, driving forces, ice types and surface conditions, which influence pond formation significantly (Liu et al., 2015; Wang et al., 2018; Li et al., 2020).

For the Fram Strait (orange) the dataset is showing the most continuous evolution (Figure 3) as it is homogeneously monitoring the same ice floes following the MOSAiC drift whose MPF evolution is discussed in Chapter 4.1. In the Canadian Arctic (red) some of the highest MPFs are detected. This is likely because the landfast ice is less deformed enabling the flooding of large areas once melt ponds are formed (Yackel et al., 2000; Landy et al., 2014; Wang et al., 2018). This might also be the reason for the heavily ponded subset in early summer (June 10) in the Siberian Arctic (blue), which is not only located at relatively low latitudes but also between the Bolshevik Island and the mainland. The results for the Siberian Arctic scatter the most and do not show a gradual evolution over the summer. For further

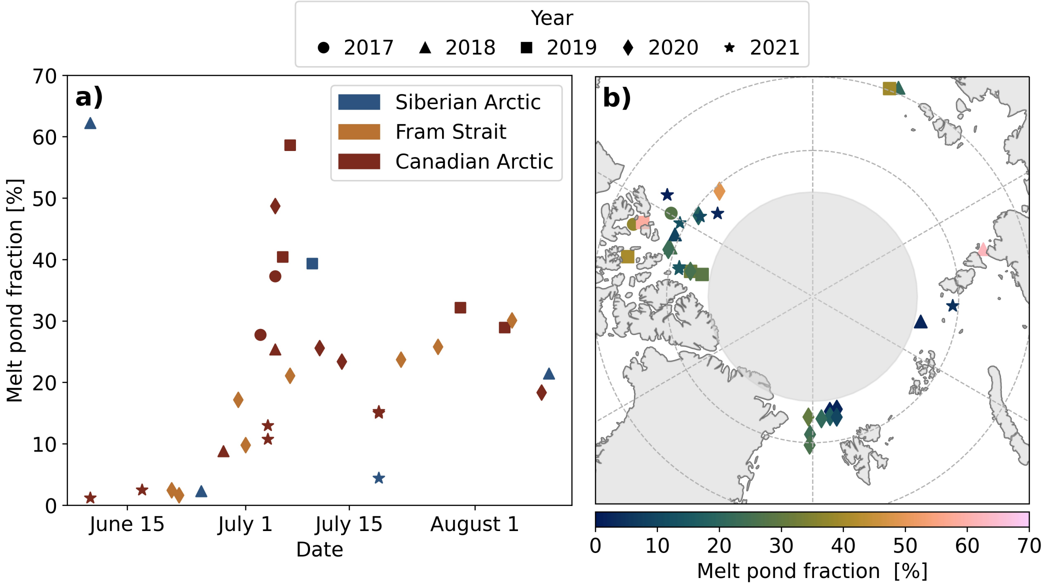

Figure 3. Sentinel-2 derived MPFs plotted against date (a) and on a pan-Arctic map (b). The shape of the markers depicts the year of observation. (a): The color of the markers shows a regional assignment into the Fram Strait and the Siberian and Canadian Arctic areas. (b): The color scale indicates the MPF, the grey circle shows the area where Sentinel-2 is not measuring.

analysis a larger amount of satellite scenes assisted by airborne measurements would be necessary as the scatter between different regions can be of similar magnitude as the scatter between different years of a particular region.

5 Conclusions

This study adds a spatial component to the in-situ analysis of melt pond evolution on the MOSAiC CO performed by Webster et al. (2022) and enables a discussion of the CO's representation of the broader vicinity. Despite the resolution of 10 m, the overall development and drainage of melt ponds is well monitored and in agreement with in-situ observations. However, the estimated uncertainty of 4 % and 6 % before and after the pond drainage, eventually exceeds the MPF differences in between days. A linear increase of uncertainty with the development of lateral and vertical drainage channels can be assumed. A strong spatial variability is observed even within the MOSAiC CO based on different ice topography, showing a segmentation of the CO into two parts: one with level ice and one with highly deformed ice. In the beginning of the melt period the MOSAiC floe is not representative for the melting in the vicinity because the high deformity of the ice was exceptional and exhibited earlier ponding. With progressing time, melt ponds also form on level ice and the MPF in the MOSAiC CO becomes increasingly similar to that in the broader vicinity. At the beginning of July the mean MPF on the CO amounts to 16 % and at the end of July, after pond drainage, to 24 %. The study of pan-Arctic MPF reveals large variability between regions and years underlining the need of improved MPF datasets. The presented algorithm can be applied to any Sentinel-2 measurements of sea ice/ocean surfaces to extract melt pond and open water fractions. The presented subsets are available on PANGAEA and can serve as reference for the validation and evaluation of low resolution pan-Arctic melt pond products.

Acronyms

CO Central Observatory
EOS Electro-Optical System
GNSS Global Navigation Satellite System
L1C Level-1C
MOSAiC Multidisciplinary drifting Observatory for the Study of Arctic Climate
MPF Melt Pond Fraction
MSI MultiSpectral Instrument
NIR Near-Infrared
RGB Red-Green-Blue
SSL Surface Scattering Layer
TOA Top Of the Atmopshere

Open Research

- The Sentinel-2 satellite imagery is available at the Copernicus Open access Hub of the European Space Agency (ESA) under: https://scihub.copernicus.eu/dhus/#/home
- The MPF product based on the Sentinel-2 imagery will be available on PANGAEA (preliminary link: https://doi.pangaea.de/10.1594/PANGAEA.950885?format=html#download)
- The optical orthomosaics are available on PANGAEA (https://doi.pangaea.de/10.1594/PANGAEA.949433)
- The OSSP-derived satellite melt pond fractions (Wright et al., 2020) for MOSAiC are available at the Arctic Data Center under: Wright, N.,Webster, M., and C. Polashenski. (2021). Melt Pond Maps around the Multidisciplinary drifting Observatory for the Study of Arctic Climate (MOSAiC) Drifting Station derived from High Resolution Optical Imagery, 2020. urn: node: ARCTIC. doi:10.18739/A2696ZZ9W

Acknowledgments

This work was funded by the German Research Foundation (DFG, Deutsche Forschungsgemeinschaft) – Project-ID 268020496 – TRR 172 within the collaborative research project $(AC)^3$ on Arctic Amplification and through the Priority Program SPP 1158, grant no. 424326801. We thank the European Space Agency for providing the Sentinel-2 satellite data. MAW conducted this work under NASA's New Investigator Program in Earth Science (80NSSC20K0658) and National Science Foundation project (2138786). MN was partly funded through the EU Horizon 2020 project Arctic Passion (101003472). Part of the data used in this article were produced as part of the international MOSAiC project with the tag MOSAiC20192020 and the Project_ID: AWI_PS122_00. We thank all people involved in the expedition of the R/V Polarstern during MOSAiC in 2019–2020, especially HeliService and their pilots, as listed in (Nixdorf et al., 2021)

References

Buckley, E. M., Farrell, S. L., Duncan, K., Connor, L. N., Kuhn, J. M., & Dominguez, R. T. (2020). Classification of sea ice summer melt features in high-resolution IceBridge imagery. *Journal of Geophysical Research: Oceans*, *125*(5), e2019JC015738.

Dorn, W., Rinke, A., Köberle, C., Dethloff, K., & Gerdes, R. (2018). HIRHAM–

NAOSIM 2.0: The upgraded version of the coupled regional atmosphere-ocean-sea ice model for Arctic climate studies. *Geoscientific Model Development Discussions*, 1–30.

Eicken, H., Grenfell, T., Perovich, D., Richter-Menge, J., & Frey, K. (2004). Hydraulic controls of summer Arctic pack ice albedo. *Journal of Geophysical Research: Oceans*, *109*(C8).

Eicken, H., Krouse, H., Kadko, D., & Perovich, D. (2002). Tracer studies of pathways and rates of meltwater transport through Arctic summer sea ice. *Journal of Geophysical Research: Oceans*, *107*(C10), SHE–22.

Flocco, D., Feltham, D. L., & Turner, A. K. (2010). Incorporation of a physically based melt pond scheme into the sea ice component of a climate model. *Journal of Geophysical Research: Oceans*, *115*(C8).

Grenfell, T. C., & Maykut, G. A. (1977). The optical properties of ice and snow in the Arctic Basin. *Journal of Glaciology*, *18*(80), 445–463.

Huang, W., Lu, P., Lei, R., Xie, H., & Li, Z. (2016). Melt pond distribution and geometry in high Arctic sea ice derived from aerial investigations. *Annals of Glaciology*, *57*(73), 105–118. doi: 10.1017/aog.2016.30

Hunke, E. C., Hebert, D. A., & Lecomte, O. (2013). Level-ice melt ponds in the Los Alamos sea ice model, CICE. *Ocean Modelling*, *71*, 26–42.

Istomina, L., Heygster, G., Huntemann, M., Marks, H., Melsheimer, C., Zege, E., … Katsev, I. (2015b). Melt pond fraction and spectral sea ice albedo retrieval from MERIS data–Part 2: Case studies and trends of sea ice albedo and melt ponds in the Arctic for years 2002–2011. *The Cryosphere*, *9*(4), 1567–1578.

Istomina, L., Heygster, G., Huntemann, M., Schwarz, P., Birnbaum, G., Scharien, R., … others (2015a). Melt pond fraction and spectral sea ice albedo retrieval from MERIS data–Part 1: Validation against in situ, aerial, and ship cruise data. *The Cryosphere*, *9*(4), 1551–1566.

Istomina, L., von Hoyningen-Huene, W., Kokhanovsky, A., & Burrows, J. (2010). The detection of cloud-free snow-covered areas using AATSR measurements. *Atmospheric Measurement Techniques*, *3*(4), 1005–1017.

Krumpen, T., von Albedyll, L., Goessling, H. F., Hendricks, S., Juhls, B., Spreen, G., … others (2021). MOSAiC drift expedition from October 2019 to July 2020: Sea ice conditions from space and comparison with previous years. *The Cryosphere*, *15*(8), 3897–3920.

Landy, J., Ehn, J., Shields, M., & Barber, D. (2014). Surface and melt pond evolution on landfast first-year sea ice in the Canadian Arctic Archipelago. *Journal of Geophysical Research: Oceans*, *119*(5), 3054–3075.

Lee, S., Stroeve, J., Tsamados, M., & Khan, A. L. (2020). Machine learning approaches to retrieve pan-Arctic melt ponds from visible satellite imagery. *Remote Sensing of Environment*, *247*, 111919.

Lei, R., Cheng, B., Hoppmann, M., Zhang, F., Zuo, G., Hutchings, J. K., … Nicolaus, M. (2022, jul). Seasonality and timing of sea ice mass balance and heat fluxes in the Arctic transpolar drift during 2019- 2020. *Elementa*, *10*(1).

Li, Q., Zhou, C., Zheng, L., Liu, T., & Yang, X. (2020). Monitoring evolution of melt ponds on first-year and multiyear sea ice in the Canadian Arctic Archipelago with optical satellite data. *Annals of Glaciology*, *61*(82), 154–163.

Light, B., Grenfell, T. C., & Perovich, D. K. (2008). Transmission and absorption of solar radiation by Arctic sea ice during the melt season. *Journal of Geophysical Research: Oceans*, *113*(C3).

Light, B., Smith, M. M., Perovich, D. K., Webster, M. A., Holland, M. M., Linhardt, F., … others (2022). Arctic sea ice albedo: Spectral composition, spatial heterogeneity, and temporal evolution observed during the MOSAiC drift. *Elem Sci Anth*, *10*(1), 000103.

Liu, J., Song, M., Horton, R. M., & Hu, Y. (2015, may). Revisiting the potential of melt pond fraction as a predictor for the seasonal Arctic sea ice extent minimum. *Environmental Research Letters*, *10*(5). doi: 10.1088/1748-9326/10/5/054017

Malinka, A., Zege, E., Heygster, G., & Istomina, L. (2016). Reflective properties of white sea ice and snow. *The Cryosphere*, *10*(6), 2541–2557.

Malinka, A., Zege, E., Istomina, L., Heygster, G., Spreen, G., Perovich, D., & Polashenski, C. (2018). Reflective properties of melt ponds on sea ice. *The Cryosphere*, *12*(6), 1921–1937.

Markus, T., Cavalieri, D. J., & Ivanoff, A. (2002). The potential of using Landsat 7 ETM+ for the classification of sea-ice surface conditions during summer. *Annals of Glaciology*, *34*, 415–419.

Maykut, G., Grenfell, T., & Weeks, W. (1992). On estimating spatial and temporal variations in the properties of ice in the polar oceans. *Journal of marine systems*, *3*(1-2), 41–72.

Miao, X., Xie, H., Ackley, S. F., Perovich, D. K., & Ke, C. (2015). Object-based detection of Arctic sea ice and melt ponds using high spatial resolution aerial photographs. *Cold Regions Science and Technology*, *119*, 211–222.

Neckel, N., Fuchs, N., Birnbaum, G., Hutter, N., Jutila, A., Buth, L., ... Haas, C. (2022). *Helicopter-borne RGB orthomosaics and photogrammetric Digital Elevation Models from the MOSAiC Expedition.* Retrieved from https://doi.pangaea.de/10.1594/PANGAEA.949433

Nicolaus, M., Katlein, C., Maslanik, J., & Hendricks, S. (2012). Changes in Arctic sea ice result in increasing light transmittance and absorption. *Geophysical Research Letters*, *39*(24).

Nicolaus, M., Perovich, D. K., Spreen, G., Granskog, M. A., von Albedyll, L., Angelopoulos, M., ... others (2022). *Overview of the MOSAiC expedition: Snow and sea ice* (Vol. 10) (No. 1). University of California Press.

Nixdorf, U., Dethloff, K., Rex, M., Shupe, M., Sommerfeld, A., Perovich, D. K., ... others (2021). MOSAiC extended acknowledgement.

Peng, Z., Ding, Y., Qu, Y., Wang, M., & Li, X. (2022). Generating a Long-Term Spatiotemporally Continuous Melt Pond Fraction Dataset for Arctic Sea Ice Using an Artificial Neural Network and a Statistical-Based Temporal Filter. *Remote Sensing*, *14*(18), 4538.

Perovich, D., Smith, M., Light, B., & Webster, M. (2021). Meltwater sources and sinks for multiyear Arctic sea ice in summer. *The Cryosphere*, *15*(9), 4517–4525. doi: 10.5194/tc-15-4517-2021

Perovich, D., Tucker III, W., & Ligett, K. (2002). Aerial observations of the evolution of ice surface conditions during summer. *Journal of Geophysical Research: Oceans*, *107*(C10), SHE–24.

Perovich, D. K., et al. (1996). The optical properties of sea ice.

Pohl, C., Istomina, L., Tietsche, S., Jäkel, E., Stapf, J., Spreen, G., & Heygster, G. (2020). Broadband albedo of Arctic sea ice from MERIS optical data. *The Cryosphere*, *14*(1), 165–182.

Polashenski, C., Perovich, D., & Courville, Z. (2012). The mechanisms of sea ice melt pond formation and evolution. *Journal of Geophysical Research: Oceans*, *117*(C1).

Rabe, B., Heuzé, C., Regnery, J., Aksenov, Y., Allerholt, J., Athanase, M., ... others (2022). *Overview of the MOSAiC expedition: Physical oceanography* (Vol. 10) (No. 1). University of California Press.

Rinke, A., Cassano, J. J., Cassano, E. N., Jaiser, R., & Handorf, D. (2021, jul). Meteorological conditions during the MOSAiC expedition: Normal or anomalous? *Elementa*, *9*(1). doi: 10.1525/elementa.2021.00023

Rösel, A., & Kaleschke, L. (2011). Comparison of different retrieval techniques for melt ponds on Arctic sea ice from Landsat and MODIS satellite data. *Annals* *of Glaciology*, *52*(57), 185–191.

Rösel, A., Kaleschke, L., & Birnbaum, G. (2012). Melt ponds on Arctic sea ice determined from MODIS satellite data using an artificial neural network. *The cryosphere*, *6*(2), 431–446.

Shupe, M. D., Rex, M., Blomquist, B., Persson, P. O. G., Schmale, J., Uttal, T., ... others (2022). *Overview of the MOSAiC expedition: Atmosphere* (Vol. 10) (No. 1). University of California Press.

Smith, M. M., Light, B., Macfarlane, A. R., Perovich, D. K., Holland, M. M., & Shupe, M. D. (2022). Sensitivity of the Arctic sea ice cover to the summer surface scattering layer. *Geophysical Research Letters*, e2022GL098349.

Thielke, L., Fuchs, N., Spreen, G., Tremblay, B., Birnbaum, G., Huntemann, M., ... Webster, M. A. (2022). Seasonal predictability of summer melt ponds from winter sea ice surface temperature.

Untersteiner, N. (1961). On the mass and heat budget of arctic sea ice. *Archiv für Meteorologie, Geophysik und Bioklimatologie, Serie A*, *12*(2), 151–182.

Wang, M., Su, J., Landy, J., Leppäranta, M., & Guan, L. (2020). A new algorithm for sea ice melt pond fraction estimation from high-resolution optical satellite imagery. *Journal of Geophysical Research: Oceans*, *125*(10), e2019JC015716.

Wang, M., Su, J., & Li, T. (2018, 11). Determination of Arctic melt pond fraction and sea ice roughness from Unmanned Aerial Vehicle (UAV) imagery. *Advances in Polar Science*, *29*, 181-189.

Webster, M. A., Holland, M., Wright, N. C., Hendricks, S., Hutter, N., Itkin, P., ... others (2022). Spatiotemporal evolution of melt ponds on Arctic sea ice: MOSAiC observations and model results. *Elem Sci Anth*, *10*(1), 000072.

Webster, M. A., Rigor, I. G., Perovich, D. K., Richter-Menge, J. A., Polashenski, C. M., & Light, B. (2015). Seasonal evolution of melt ponds on Arctic sea ice. *Journal of Geophysical Research: Oceans*, *120*(9), 5968–5982.

Wright, N., & Polashenski, C. (2019). *Open Source Sea-ice Processing Algorithm v2.3.* Zenodo. Retrieved from `https://doi.org/10.5281/zenodo.3551033` doi: 10.5281/zenodo.3551033

Wright, N., & Polashenski, C. (2020). How Machine Learning and High-Resolution Imagery Can Improve Melt Pond Retrieval From MODIS Over Current Spectral Unmixing Techniques. *Journal of Geophysical Research: Oceans*, *125*.

Wright, N., Webster, M., & Polashenski, C. (2021). *Melt Pond Maps around the Multidisciplinary drifting Observatory for the Study of Arctic Climate (MOSAiC) Drifting Station derived from High Resolution Optical Imagery, 2020.* Retrieved from `https://arcticdata.io/catalog/view/doi:10.18739/A2696ZZ9W` doi: doi:10.18739/A2696ZZ9W

Yackel, J. J., Barber, D. G., & Hanesiak, J. M. (2000, sep). Melt ponds on sea ice in the Canadian Archipelago: 1. Variability in morphological and radiative properties. *Journal of Geophysical Research: Oceans*, *105*(C9), 22049–22060. doi: 10.1029/2000jc900075

Zege, E., Malinka, A., Katsev, I., Prikhach, A., Heygster, G., Istomina, L., ... Schwarz, P. (2015). Algorithm to retrieve the melt pond fraction and the spectral albedo of Arctic summer ice from satellite optical data. *Remote Sensing of Environment*, *163*, 153–164. Retrieved from `http://dx.doi.org/10.1016/j.rse.2015.03.012`